# *DEMONSTRATION OF THE USE OF SYNTHETIC APERTURE RADAR-DETERMINED WIND SPEED IN NUMERICAL WEATHER PREDICTION ERROR DETECTION*

**Nathaniel S. Winstead**
The Johns Hopkins University Applied Physics Laboratory
Laurel, Maryland

**George S. Young**
The Pennsylvania State University
University Park, Pennsylvania

**Todd D. Sikora**
Millersville University
Millersville, Pennsylvania

## *Abstract*

Synthetic aperture radar-determined wind speed (SDWS) data are compared to Weather Research and Forecasting (WRF) model output for a number of meteorological phenomena in order to demonstrate how the former may be used to assess WRF errors. Fifteen cases for the Gulf of Alaska and Bering Sea are examined using a statistical approach. For that statistical approach, three aspects of WRF's wind speed output are evaluated: magnitude of error, pattern matching, and gale warning. In addition to the statistical approach, two of the cases are highlighted using an image analysis approach. It is demonstrated that SDWS can be employed to provide real-time quantification of model forecast errors. It is also demonstrated that SDWS images can be qualitatively employed to both corroborate and refute specific WRF-forecasted mesoscale phenomena. These two capabilities can be used by operational forecasters to assess the performance of an individual model run and to suggest corrections to the model's forecasts for later valid times.

Corresponding Author: Nathaniel S. Winstead
Johns Hopkins University Applied Physics Lab
11100 Johns Hopkins Road, Laurel, MD, 20723
e-mail: Nathaniel.winstead@jhuapl.edu

## 1. Introduction

The detection of errors in numerical weather prediction (NWP) model wind field (speed and direction) forecasts at sea is complicated by the relative dearth of in situ observations. Aloft, this issue can be addressed in part by using cloud-track wind fields and automated aircraft reports (e.g., Benjamin et al. 1999). Spaceborne scatterometers such as ASCAT (Figa-Saldaña et al. 2002) and passive techniques (e.g., Bessho et al. 2006, Uhlhorn et al. 2007) offer the primary means of diagnosing the oceanic surface wind field. (Herein, surface wind is that at 10 m above sea level and will be referred to simply as wind.) In both cases, the remote sensing observation and model forecast are not completely independent; these observations are also assimilated into many over-ocean NWP models. Both sensor systems also suffer from relatively low spatial resolution (10s of kilometers), which limits their ability to detect many mesoscale features and to be employed near coasts. Because it produces higher-resolution imagery, spaceborne synthetic aperture radar (SAR) offers the potential to address this resolution issue, although SAR introduces other complications that are discussed below.

One objective of this study is to demonstrate how SAR-determined wind speed (SDWS) data can provide operational forecasters with quantitative error statistics for domains of the Weather Research and Forecasting (WRF) Model system's Advanced Research WRF version 3.2 (hereafter, simply WRF) (Skamarock et al. 2008). Another objective is to demonstrate that SDWS images can give operational forecasters qualitative indication of WRF performance in terms of weather feature replication and placement. The techniques presented herein can be applied to any nested-grid NWP model, but are most applicable to those run at high resolution. The operational utility of SDWS-based NWP model error detection is facilitated by, for example, the National Oceanic and Atmospheric Administration's (NOAA's) SAR wind products (Pichel et al. 2011, available soon through NOAA CoastWatch, http://coastWatch.noaa.gov, W. G. Pichel, 2012, personal communication) and by the Canadian National SAR Winds Project (Khurshid et al. 2012).

Demonstration of SDWS-based error detection for WRF forecasts is conducted in this study using a set of cases selected from the SDWS image archive at Johns Hopkins University Applied Physics Laboratory (http://fermi.jhuapl.edu/SAR/stormwatch/web_wind/). These cases were selected to provide clear cut examples of those weather phenomena that are frequently accompanied by strong wind speed and wind direction variability in the study region (Table 1). The period of study was determined by the availability of SAR imagery of appropriate swath width and resolution. The SAR employed in this study is

| Date | Time (UTC) | Lat. (degrees) | Long. (degrees) | Weather Phenomena |
|---|---|---|---|---|
| 12/18/2007 | 0250 | 57.84N | 138.71W | Hybrid exit jet / barrier jet |
| 12/30/2007 | 0340 | 57.86N | 151.29W | Exit jet |
| 1/1/2008 | 1807 | 56.55N | 177.48W | Warm front and cold conveyor belt with shear-driven gravity waves |
| 1/5/2008 | 0545 | 53.85N | 178.64E | Warm front and cold conveyor belt |
| 1/6/2008 | 0336 | 57.86N | 150.24W | Exit jet |
| 1/7/2008 | 1651 | 55.72N | 158.82W | Orographic gravity waves |
| 1/8/2008 | 0558 | 56.67N | 174.53E | Warm front |
| 1/13/2008 | 0332 | 57.46N | 149.02W | Front |
| 1/24/2008 | 1836 | 57.34N | 175.48E | Secluded cyclone |
| 1/26/2008 | 0532 | 53.05N | 177.94E | Orographic gravity waves |
| 1/29/2008 | 0546 | 57.84N | 177.23E | Cold front and barrier jet |
| 2/9/2008 | 0523 | 49.44N | 174.76W | Prefrontal jet with shear-driven gravity waves |
| 2/17/2008 | 0450 | 53.85N | 167.72W | Orographic gravity waves superposed on exit jet |
| 2/27/2008 | 0318 | 53.03N | 144.38W | Secluded cyclone |
| 3/14/2008 | 0532 | 53.05N | 177.95W | Orographic gravity waves |

**Table 1.** Case descriptions.

that aboard RADARSAT-1 (http://www.asc-csa.gc.ca/eng/satellites/radarsat1/). This SAR is C-band and employs HH polarization. This study is focused on the Gulf of Alaska and Bering Sea.

## 2. Synthetic Aperture Radar-Determined Wind Speed

SAR data can be used to determine wind speed in much the same way as scatterometer data is used: by inverting the radar backscatter from small waves on the ocean surface (Stoffelen and Anderson 1993, 1997). The calculation of SDWS is usually undertaken using semi-empirical algorithms such as CMOD4 (e.g., Freilich and Dunbar 1999, Stoffelen and Anderson 1993) and CMOD5 (Hersbach et al. 2007). While these algorithms were originally developed for vertically polarized spaceborne scatterometers, most have been modified for use with horizontally polarized SARs (e.g. Thompson and Beal 2000, Thompson et al. 2001). In most cases, the results compare well with in situ and scatterometer observations (e.g., Horstmann et al. 2003, Monaldo et al. 2001, 2004, Fisher et al. 2008).

For the C-band (approximately 5.6 cm wavelength) SARs used in this study, the signal is backscattered primarily by wind-driven waves of a few centimeters wavelength. The inversion is possible because the amplitude of these short waves responds quickly to changes in wind speed (larger wind speed yields larger wave amplitude), thus changing the SAR backscatter that is created through a Bragg-like resonance (Holt 2004). The relevant wave age is on the order of seconds to 10s of seconds. Thus, fetch is not an issue on large bodies of water. That rapid response, coupled with the high spatial resolution of most satellite-borne SARs, allows for mapping of wind speed at resolutions of hundreds of meters.

The inversion to obtain SDWS depends on the radar look direction relative to the wave crests and, hence, the wind direction. This is because SAR backscatter intensity varies with the direction of the incident beam relative to the scattering wave's orientation. Thus, when obtaining SDWS from backscatter data, information about wind direction is required. While for satellite-borne scatterometers such as ASCAT, the problem is neatly solved by using multiple look directions that allow simultaneous diagnosis of both wind direction (with a limited degree of ambiguity) and speed, SAR sacrifices that capability as a result of the antenna configuration and processing techniques that are directly responsible for its superior spatial resolution capabilities (Monaldo et al. 2004).

A variety of wind direction data have been used by researchers. Some deduce the wind direction from the SAR backscatter by observing the signatures of island shadows and of planetary boundary layer streaks (e.g. Gerling 1986, Wackermann et al. 1996, Fetterer et al. 1998, Horstmann et al. 2000, Koch and Feser 2006). This study followed the operational approach of NOAA's SAR wind product using NWP model data to provide the wind directions (e.g., Monaldo et al. 2001). This procedure offers the operational advantage of global coverage. The NWP model wind directions used for this study were from the same WRF scenes for which comparisons to SDWS were made. Thus, the SDWS data employed herein are not independent of the corresponding WRF wind field. The implications of this fact, both pro and con, are discussed below.

## 3. WRF

WRF was chosen for this study because it is typical of cutting edge operational NWP models (e.g., Schroeder et al. 2006, Davis et al. 2008, Wedam et al. 2009, Clark et al. 2010). To demonstrate the degree to which errors in position, intensity, and structure in synoptic and mesoscale phenomena can be detected by SDWS, WRF was run with a two-way nested grid spanning the full range of scales from the synoptic scale down to the lower end of the mesoscale. The grid spacing for the four grids was 54 km, 18 km, 6 km and 2 km. The outermost (course resolution) grid spanned over 5000 km (94×94 grid) while the innermost grid spanned almost 700 km (342×342 grid).

WRF was initialized with a cold start using Global Forecasting System-based final analysis files (obtained from http://dss.ucar.edu/datasets/ds083.2/) for initial conditions and for boundary conditions on the coarse grid. Because of the cold start and advection of features into fine-grid domains, mesoscale phenomena and the mesoscale details of synoptic-scale phenomena had to develop during the course of the WRF run. Thus, WRF runs were initiated approximately 36 hours before the comparison SDWS data.

WRF was configured with 50 vertical grid points and used the WRF 6-moment radiation scheme (Hong and Lim 2006), Yonsei University planetary boundary layer parameterization (Hong et al. 2006), the Rapid Radiative Transfer Model longwave radiation scheme (Mlawer et al. 1997), and the Dudhia shortwave radiation parameterization (Dudhia 1989). The Kain-Fritsch (Kain 2004) convective scheme was used on all but the finest grid. To avoid competition between parameterized and grid-allowed convection, there was no convective parameterization on the finest grid (Deng and Stauffer 2006). The 2-km spacing of the finest grid proved sufficient to allow convection as suggested by prior studies of deep moist convection (e.g., Coniglio et al. 2010). It was deemed necessary to reduce the fine-grid

resolution to half that used by the National Severe Storms Laboratory (Coniglio et al. 2010) because the depth, and presumably diameter, of precipitating convection in the Gulf of Alaska and Bering Sea is approximately half that typical in the southern Great Plains (Young et al. 2007, Sikora et al. 2011).

WRF's configuration was not specifically tuned for the particular cases studied. Rather, it was configured as an operational NWP model would be for appropriate representation of the regionally expected synoptic-scale and mesoscale phenomena. WRF was used solely to demonstrate the utility of SDWS for detecting errors in NWP mesoscale wind forecasts at sea and in close proximity to coasts.

## 4. Analysis Method

The use of WRF wind directions in calculating SDWS provides guaranteed availability of wind direction data. However, its use results in five possible outcomes of a SDWS-based WRF wind speed comparison (assuming that the SAR scene is not contaminated with surfactants, sea ice, slicks, etc., Holt 2004). First, the SDWS and WRF wind speed can agree because both the WRF wind speed and wind direction are correct. In this situation, the SDWS is correct because the WRF wind direction is correct, and thus the SDWS matches the WRF wind speed. Second, the SDWS and WRF wind speed can disagree because the WRF wind direction is correct, and hence the SDWS is correct, but the WRF wind speed is incorrect. Third, the SDWS and WRF wind speed can disagree because the WRF wind speed is correct but, because the WRF wind direction is incorrect, the SDWS is also incorrect. Fourth, SDWS and WRF wind speeds can disagree because both the WRF wind speed and direction are incorrect. Finally, under fortuitous combinations of WRF wind speed and wind direction errors, the SDWS may equal the WRF wind speed. Thus, in this unlikely circumstance, the incorrect SDWS and WRF wind speed will match. Without independent and correct wind direction data, there is no way to distinguish between the second, third, and fourth outcomes or between the first and fifth outcomes. Nor is there a means of reducing the number of outcomes because there is no guarantee of correct wind directions from any global source. This fact further justifies the use of WRF wind directions for generating SDWS. Moreover, that use allows SDWS to serve as a check on WRF wind directions as well as wind speeds, increasing its operational utility.

The analysis was conducted in two ways. First, traditional error statistics (Wilks 2011) were computed for wind speed for each case. This type of analysis can be employed by operational forecasters to provide real-time quantification of WRF forecast errors aggregated over the model domain. Second, SDWS images were compared qualitatively with corresponding images from each of the four WRF nested grids for two cases. This type of analysis can be employed by operational forecasters to both corroborate and refute specific WRF-forecasted mesoscale phenomena, much in the same way qualitative corrections are made in the face of traditional, but coarse, satellite data.

Although the overarching objective of this study is to demonstrate the use of SDWS in detecting WRF wind errors, for each case WRF was run in four configurations: grid 1, grids 1 and 2, grids 1, 2, and 3, and grids 1, 2, 3, and 4. This set of experiments allowed for the examination of the dependence of the forecast weather features on grid resolution and for the degree to which two-way nesting impacts the success of the larger-scale domains through upscale feedback. Results are shown only for the four-grid configuration, with discussion of upscale feedback mentioned where warranted.

## 5. Results

### a. *Statistics*

For this portion of the study, a number of traditional NWP model error statistics were computed. The SDWS was used as the comparison observation for WRF wind speed forecasts interpolated to the SDWS grid. In order to determine the extent to which the WRF errors are caused by features occurring below WRF's spatial resolution, error statistics were also computed using SDWS that was low-pass Gaussian filtered (LPF) to WRF's resolution.

Three aspects of WRF's wind speed output are evaluated: magnitude of error, pattern matching, and gale warning. The magnitude of WRF's wind speed error is evaluated using the bias, mean absolute error (MAE), and the median absolute value (MAV). Bias is simply the spatial average of the difference between the WRF wind speed and the SDWS. The MAE is the corresponding average of the absolute value of this difference. MAE is used instead of mean square error because it is not safe to assume that wind speed error is normally distributed. MAV is the median magnitude of the difference between the SDWS and the LPF SDWS. Values of these statistics are, of course, independent between cases but reflect the spatial coherence of error patterns within cases.

Even in the presence of magnitude errors, an NWP model may capture the spatial pattern of wind variation (e.g., a cyclone is in the right place but too weak). The correlation coefficient is used to assess the degree of pattern matching between the WRF wind speed and that SDWS.

Gale warning is examined because mesoscale NWP models are frequently used to support severe weather

prediction, an application appropriate to the high-latitude oceans. All of the statistics discussed for this application evaluate a binary variable: whether or not the wind speed has reached the gale limit. The gale warning comparison uses only the raw SDWS because the LPF decreases the area of gales and often eliminates gale areas. The gale warning statistics computed are the Hit Rate (i.e., the percentage of SDWS gale pixels that are also WRF gale pixels), the Threat Score, Probability of Detection, False Alarm Rate, Heidke Skill Score, and Pierce Skill Score. All of these statistics are defined in Wilks (2011).

Table 2 details the results of the statistics described above. It is important to recall that for all of these statistics, the factor of wind direction error is indistinguishable from wind speed error in our SDWS-based analysis.

WRF's bias is under 1 $ms^{-1}$ for all resolutions and shows no consistent trend with respect to resolution. This result suggests that the SDWS algorithm is well calibrated and that there is little systematic bias in WRF wind directions as either miscalibaration or direction bias would result in significant bias in the SAR wind speed retrieval. The former is to be expected given the calibration efforts that went into the CMOD5 algorithm (Hersbach et al. 2007) and the relatively small bias values reported by Fisher et al. (2008). The latter might also be expected given that any errors in turbulence parameterizations would tend to affect the turning of winds from any direction and hence introduce no bias. Filtering the SDWS field to the WRF resolution has little impact on the bias, suggesting that the bias that occurs is on the resolved scale rather than on the smaller scales removed by the filter.

In contrast, the WRF MAE is markedly larger than the buoy MAE for the same region (see Fisher et al. 2008), suggesting that MAE includes a contribution from WRF error in either wind speed or direction. The MAE increases slightly, but monotonically, as the resolution of the innermost domain is improved from 54 km to 2 km.

The potential impact of resolution on WRF wind speed accuracy can be examined from the MAV, which decreases monotonically as the degree of LPF is reduced. This trend indicates the potential ability of finer grids to resolve more of the horizontal heterogeneity in wind speed. It also reflects the MAE that can be expected from a perfect NWP model.

Pattern matching via correlation between SDWS and WRF wind speed provides yet another perspective on the resolution dependence. While the correlation coefficient never approaches 1, it does improve markedly as the resolution is improved from 54 km to 18 km in the innermost domain. Further improvement in resolution yields a much smaller increase in correlation coefficient. It is interesting that the pattern correspondence, as captured by the correlation coefficient, is largest at the resolution for which MAE is largest. This finding suggests that 2-km resolution allows WRF to place mesoscale features well, but not to assess their intensity with particular accuracy. Correlation of WRF wind speed with the LPF SDWS is somewhat better, but retains this same trend with respect to WRF resolution.

Turning to the gale warning statistics for this 15-case sample, gale warning accuracy is not particularly sensitive to WRF resolution. This result reflects the general synoptic

| Statistic | 2 km | 6 km | 18 km | 54 km |
|---|---|---|---|---|
| Bias | -0.91 | -0.64 | -0.73 | -0.99 |
| Bias for LPF SDWS | -0.90 | -0.64 | -0.76 | -1.01 |
| MAE | 3.04 | 2.91 | 2.87 | 2.80 |
| MAV | 1.14 | 1.22 | 1.36 | 1.64 |
| Correlation Coefficient | 0.48 | 0.47 | 0.45 | 0.36 |
| Correlation with LPF SDWS | 0.53 | 0.53 | 0.52 | 0.45 |
| Gale Hit Rate | 0.91 | 0.92 | 0.92 | 0.93 |
| Gale Threat Score | 0.34 | 0.35 | 0.34 | 0.34 |
| Gale Probability of Detection | 0.45 | 0.46 | 0.45 | 0.44 |
| Gale False Alarm Rate | 0.42 | 0.42 | 0.43 | 0.42 |
| Gale Heidke Skill Score | 0.47 | 0.50 | 0.47 | 0.46 |
| Gale Pierce Skill Score | 0.44 | 0.49 | 0.43 | 0.41 |

**Table 2:** Comparison statistics computed from the 15-case sample. All statistics were computed relative to the raw SDWS unless otherwise noted. LPF SDWS indicates that the SDWS was low-pass filtered to the WRF resolution. Column headings denote the grid resolution of the innermost WRF domain.

scale of gale regions in the Gulf of Alaska and Bering Sea despite the abundance of intense mesoscale phenomena.

b. *Image analysis*

Two of the cases from Table 1 are discussed here in greater detail to illustrate how SDWS imagery can be used to diagnose errors in the type, intensity, and placement of weather phenomena whose wind field is forecast by WRF. The first example is a case in which WRF's synoptic forecast was essentially correct while the second example is a case in which WRF's synoptic forecast exhibited errors sufficient to distort its mesoscale response. Both case studies include interpretation of the SDWS image and analysis of the evolution of WRF's corresponding wind field with increasing grid resolution.

### 1) Case study 1: Correct forecast of synoptic feature location

The SDWS image for 0532 UTC 26 January 2008 is shown in Fig. 1. The synoptic situation involved a large occluded cyclone that approached the Aleutian Islands from the southwest. The cyclone's conveyor belt (Carlson 1980) flowed south to north through this mountainous island chain, leading to the high winds, island wakes (e.g. Schär and Smith 1993, Grubišić et al. 1995), and horizontally propagating mountain lee waves (Grubišić and Billings 2008, Li et al. 2011) that dominate the SDWS image.

This image is thus rich in mesoscale features whose narrowest dimensions are a few kilometers. Phenomena of this scale should pose a challenge to WRF, particularly on the coarser grids. WRF had two advantages in this situation. First, WRF correctly handled the conveyor belt that drove the mesoscale phenomena and, second, many of the mesoscale features were induced by fixed terrain.

As expected, the mountain waves and island wakes are not resolved on the 54-km grid domain (Fig. 2) or on the 18-km grid domain (Fig. 3). The improved resolution of the 6-km grid domain (Fig. 4) allows WRF to resolve the Aleutian volcanoes to at least a certain extent, but the atmospheric response includes only blurred versions of the linear wakes and a suggestion of horizontally propagating lee waves with a rather long wavelength. The critical resolution is reached on the fourth nested domain with its 2-km grid (Fig. 5). On this domain, the mesoscale structures observed on SDWS images are readily apparent. Indeed, the WRF results suggest that the banded wave pattern is the result of the superposition of numerous V-shaped isolated-peak lee waves rather than classic flow-over-ridge lee waves. That pattern, which makes sense given the volcanic terrain, can be seen clearly in the southwest quadrant of Fig. 5.

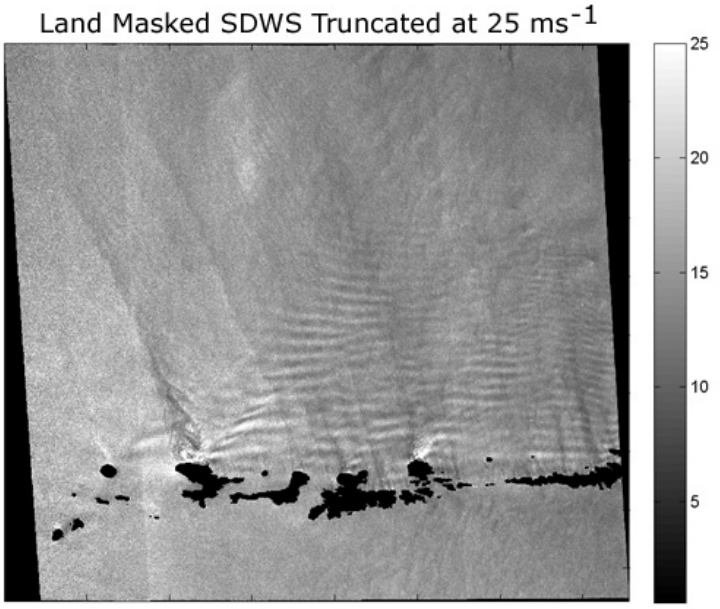


**Fig. 1.** SDWS image derived from a Radarsat-1 HH-pol synthetic aperture radar image collected at 0532 UTC 26 January 2008. Wind speeds are shown in $ms^{-1}$. The spatial resolution of the SDWS image is 250 m. The image is located in the southern Bering Sea just north of the Aleutian Islands. The islands have been masked so that complex terrain would not be misinterpreted as wind patterns. The quasi-linear alternating pattern of high and low wind speeds oriented approximately parallel with the Aleutian Islands are the surface expressions of orographically induced atmospheric internal gravity waves.

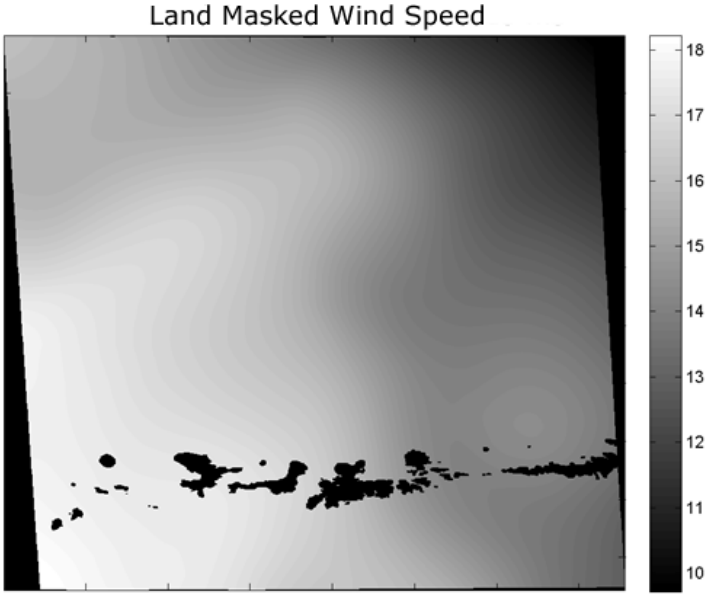


**Fig. 2.** WRF 54-km grid domain surface wind speed for 0532 UTC 26 January 2008 in $ms^{-1}$.

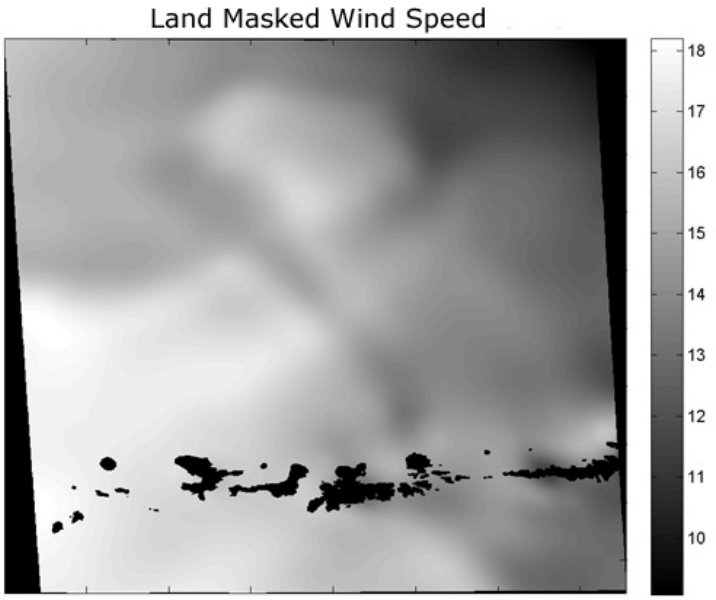


**Fig. 3.** Same as Fig. 2 except for 18-km WRF domain.

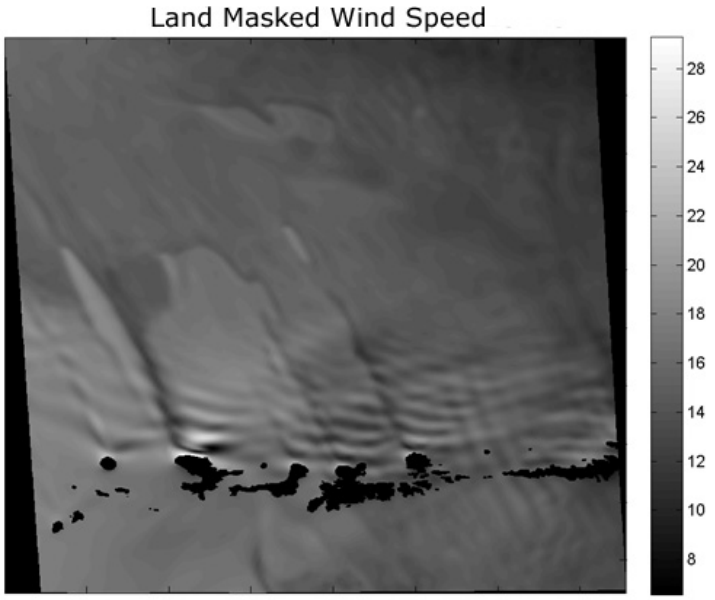


**Fig. 5.** Same as Fig. 2 except for 2-km grid domain.

This case affirms that when WRF correctly predicts the synoptic scale structure and evolution, it has the potential for achieving accurate forecasts of terrain-induced mesoscale flows at scales far smaller than those resolved in the initial conditions. This study is by no means the first to note this trait of NWP models to the operational forecasting community (e.g., Wetzel et al. 2001, Cairns and Corey 2003). The key insight here is that SDWS images can be used to corroborate the WRF forecast of such features. The next case study demonstrates the need for such a diagnostic check before accepting the mesoscale details of a synoptically initialized forecast.

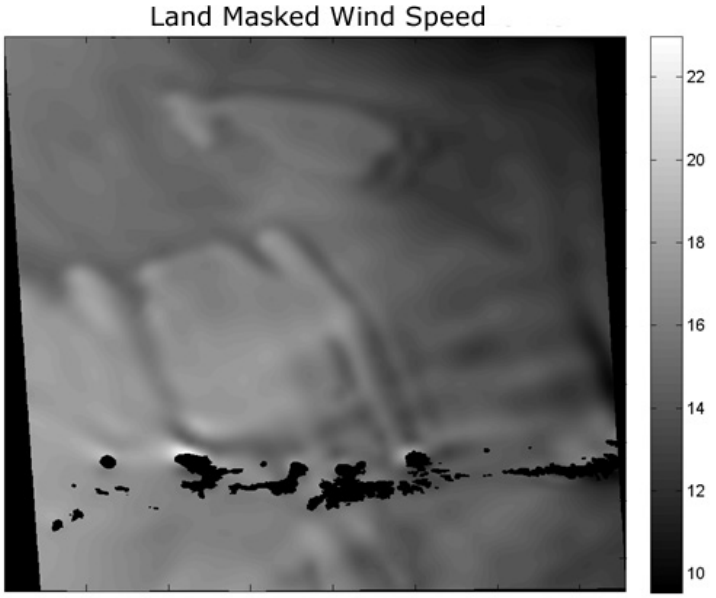


**Fig. 4.** Same as Fig. 2 except for 6-km grid domain.

## 2) Case study 2: Incorrect forecast of synoptic forecast location

The SDWS image for 0332 UTC 13 January 2008 is shown in Fig. 6. The synoptic situation is a landfalling secluded cyclone in the north-central Gulf of Alaska. As the secluded cyclone moved inland, one mesoscale lobe of low pressure along the coast separated and remained adjacent to a merged gap flow exit jet. The SDWS image captures this mesoscale cyclone, its offshore mesoscale

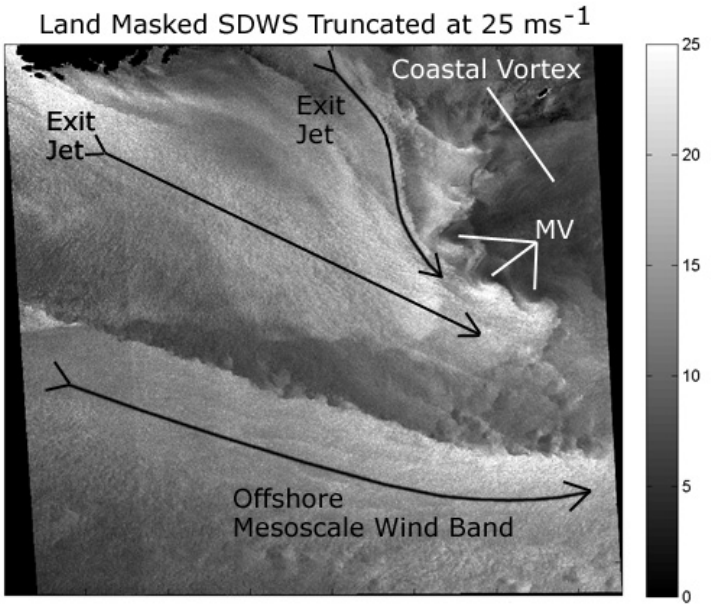


**Fig. 6.** SDWS image for 0332 UTC 13 January 2008. Wind speeds are shown in $ms^{-1}$. The spatial resolution of the SDWS image is 250 m. The image is located in the southern Gulf of Alaska. Land has been masked so that complex terrain would not be misinterpreted as wind patterns. MV signifies mesovortices.

wind band, the merging of two exit jets, and additional mesovortices along the sharp shear line that forms the eastern edge of the merged exit jet. The SDWS image also captures smaller exit jets between the two primary exit jets that are labeled in Fig. 6.

SDWS error detection of WRF for this case breaks into two components. First is the existence and location of the primary mesoscale features: the mesoscale cyclone, its offshore mesoscale wind band, and the merged exit jet. This component depends to a large extent on how well WRF has predicted the synoptic flow. The second component is whether the interaction of the mesoscale flow leads to the correct structure and placement of the secondary mesoscale phenomena, such as the mesovortices observed along the eastern edge of the merged exit jet. This second component poses the greatest challenge because these phenomena are not directly tied to terrain features.

The mesoscale cyclone is absent on the 54-km and 18-km grid domains (Figs. 7 and 8, respectively). But, WRF succeeds in predicting the existence, size, and intensity of the mesoscale cyclone on the 6-km and 2-km grid domains to the limit of their grid resolution (Figs. 9 and 10, respectively). With its greater resolution, the 18-km grid domain shows the sharp north-south oriented wind speed edge to the eastern exit jet. Interestingly, the 18-km grid domain does a poorer job of mesoscale feature placement when run as the smallest scale domain, but does better when allowed feedback from the 6-km grid

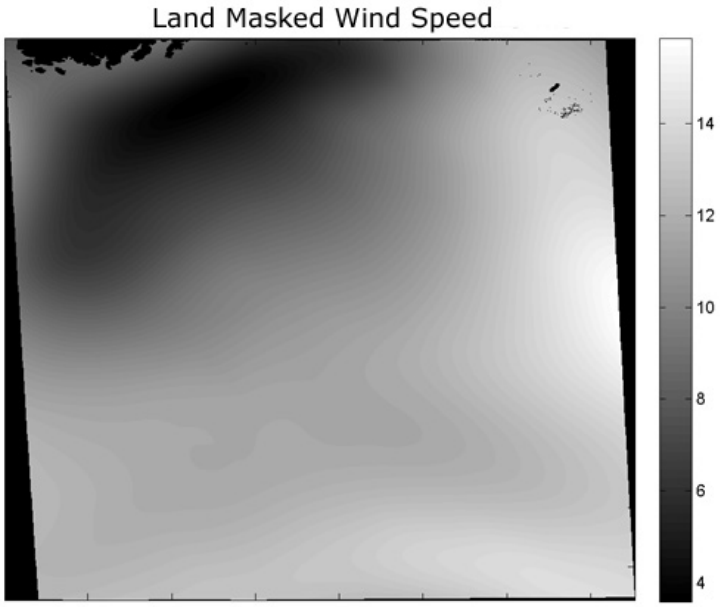


**Fig. 7.** WRF 54-km grid domain surface wind speed for 0332 UTC 13 January 2008 in $ms^{-1}$.

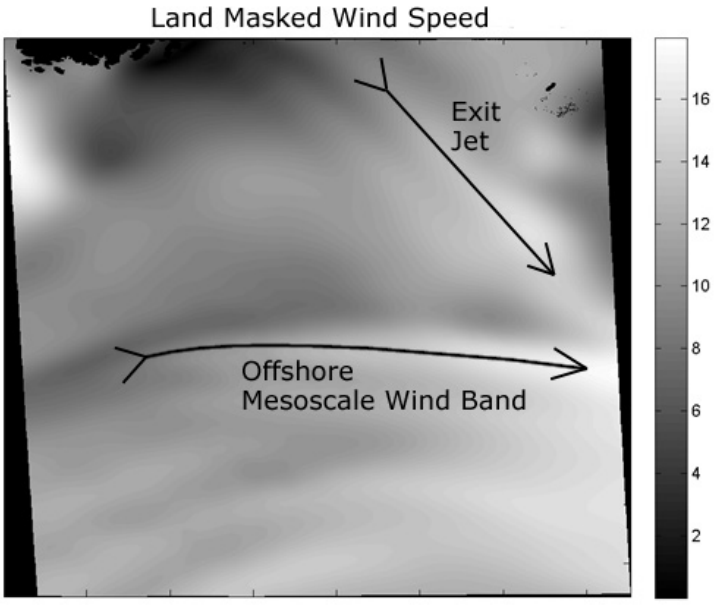


**Fig. 8.** Same as Fig. 7 except for 18-km grid domain.

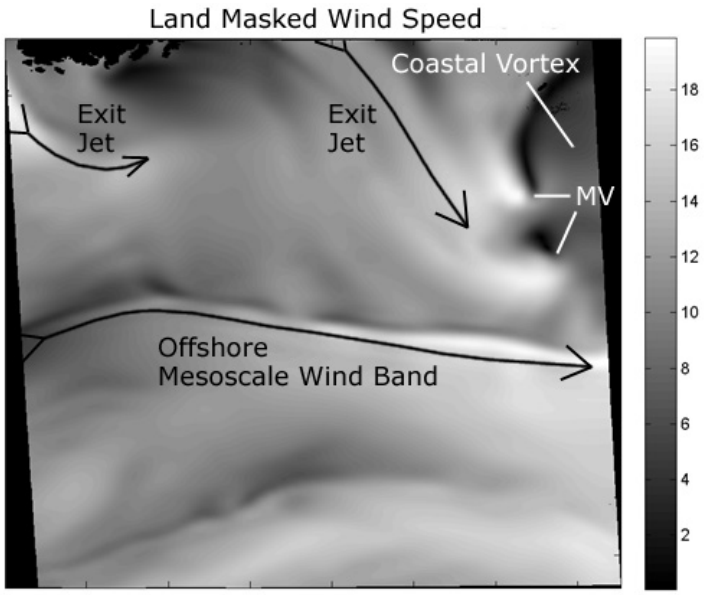


**Fig. 9.** Same as Fig. 7 except for 6-km grid domain.

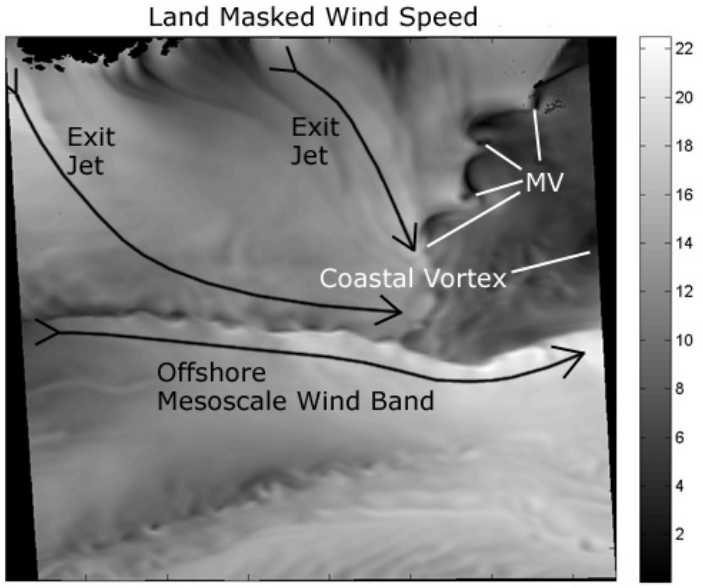


**Fig. 10**. Same as Fig. 7 except for 2-km grid domain. MV is mesovortices.

domain (not shown). In contrast, the 6-km grid domain places most of the features in about the right locations whether or not it is allowed feedback from the 2-km grid domain.

The 2-km grid domain does a spectacular job of resolving the interactions of the two primary exit jets, including the leading edge of the merged exit jet and its mesovortices. On the 2-km grid, WRF shows the roughly east-west shear line across the middle of the SDWS image that forms the southern edge of the western exit jet and the north-northeast to south-southwest shear line that forms the eastern edge of the eastern exit jet. The western end of the first shear line is nearly perfectly positioned while the eastern end is displaced northward by a quarter of the image height (approximately 125 km). Likewise, the second shear line crosses the image boundary at the correct location, but is not as tightly curved as it is in the SDWS image. Thus, both shear lines are correctly positioned at their landward ends but become displaced farther into WRF's innermost domain. A similar effect is seen with the smaller exit jets, with the landward ends of these phenomena tied to the correct terrain features but the seaward tails of some being displaced. This behavior suggests that WRF had some error in the synoptic scale flow field that was feeding downscale into the terrain-driven mesoscale flows.

As a result of these errors and the chaotic nature of shear-driven turbulence, the mesovortices were not correctly positioned either (compare Figs. 6 and 10). Rather remarkably, though, their scale and structure corresponded well to those seen in the SDWS image. This case illustrates that with sufficient resolution, WRF can capture the existence and approximate structure of mesoscale phenomenon even when its predictions of placement are incorrect. Again, this is well known to the operational forecasting community. The key insight here is that SDWS images can play an important role in both corroborating and refuting the existence, intensity, and placement of WRF-forecasted mesoscale phenomena.

## 6. Summary and Recommendations

The use of SDWS in detecting WRF wind errors was demonstrated using two approaches. The first was a statistical analysis. For the 15 WRF cases examined here, increased WRF resolution improved the positioning of weather features but not their intensity. This type of analysis can be employed operationally to provide forecasters with a quantitative indication of when an NWP model is performing poorly across its domain, a tool suitable for real-time warning of forecast errors. Second, two case studies were presented to demonstrate how SDWS images can be used qualitatively to corroborate and refute NWP model forecasts of specific weather features. Although this study focused on WRF, the techniques presented herein can be applied to any nested-grid NWP model.

This study focused on the Gulf of Alaska and Bering Sea. Future work should extend this type of demonstration to other marine regions, such as the tropics and mid-latitudes. Future work should also exploit SDWS to investigate the ability of mesoscale NWP models to depict specific phenomena. For example, SDWS observations of the size, intensity, and orientation of the gust/lull wakes of precipitating convection (Young et al. 2007, Sikora et al. 2011) can be used to determine the ability of convective downdraft parameterizations and grid-resolved convective downdrafts to create realistic convective wakes and, hence, air-sea fluxes.

## Authors

***Dr. Nathaniel S. Winstead*** is a senior staff meteorologist at the Johns Hopkins University Applied Physics Laboratory. Dr. Winstead received his B.S. (1993) from Duke University and his M.S. (1995) and Ph.D. (1999) from Penn State. His research interests include numerical weather prediction, the structure and dynamics of mesoscale meteorological phenomena and the active remote sensing of the oceans using synthetic aperture radar and scatterometery.

***Dr. George S. Young*** is a professor of meteorology at Penn State. Dr. Young received his B.S. (1979) and M.S. (1982) from Florida State University and his Ph.D. (1986) from Colorado State University. His teaching interests include the structure and dynamics of atmospheric flows on all scales and the applications of computation and statistics to predictive and commercial meteorology. Dr. Young's research spans a similar range with concentrations in mesoscale meteorology, mountain meteorology, boundary layer meteorology, marine meteorology, ornithological meteorology, statistical meteorology, and the economic value of weather data and forecasts.

***Dr. Todd D. Sikora*** is a professor of meteorology at Millersville University. Dr. Sikora received his B.S. (1990), M.S. (1992), and Ph.D. (1996) in meteorology from Penn State. Dr. Sikora's teaching interests include synoptic meteorology, mesoscale meteorology, and weather analysis and forecasting. Dr. Sikora's research is focused on air-sea interaction and ocean remote sensing.

**Acknowledgments**

This work was supported in part by grants ATM-0240869 and ATM-0240269 from the National Science Foundation and grants N00014-10-1-0569, N00014-07-1-0934, N000 14-07-1-0577, and N00014-06-1-0046 from the Office of Naval Research.

References

Benjamin, S. G., B. E. Schwartz, and R. E. Cole, 1999: Accuracy of ACARS wind and temperature observations determined by collocation. *Wea. Forecasting*, 14, 1032–1038.

Bessho, K., M. DeMaria, and J. A. Knaff, 2006: Tropical cyclone wind retrievals from the advanced microwave sounding unit: application to surface wind analysis. *J. Appl. Meteorol. Climatol.*, 45, 399–415.

Cairns, M. M., and J. Corey, 2003: Mesoscale model simulations of high-wind events in the complex terrain of western Nevada. *Wea. Forecasting*, 18, 249–263.

Carlson, T. N., 1980: Airflow through midlatitude cyclones and the comma cloud pattern. *Mon. Wea. Rev.*, 108, 1498–1509.

Clark, A. J., W. A. Gallus, and M. L. Weisman, 2010: Neighborhood-based verification of precipitation forecasts from convection-allowing NCAR WRF model simulations and the operational NAM. *Wea. Forecasting*, 25, 1495–1509.

Coniglio, M. C., K. L. Elmore, J. S. Kain, S. J. Weiss, M. Xue, and M. L. Weisman, 2010: Evaluation of WRF model output for severe weather forecasting from the 2008 NOAA Hazardous Weather Testbed Spring Experiment. *Wea. Forecasting*, 25, 408–427.

Davis, C., and coauthors, 2008: Prediction of landfalling hurricanes with the advanced hurricane WRF model. *Mon. Wea. Rev*., 136, 1990–2005.

Deng, A., and D. R. Stauffer, 2006: On improving 4-km mesoscale model simulations. *J. Appl. Meteorol. Climatol.*, 45, 361–381.

Dudhia, J., 1989: Numerical study of convection observed during the winter monsoon experiment using a mesoscale two-dimensional model. *J. Atmos. Sci.*, 46, 3077–3107.

Fetterer, F., D. Gineris, and C. C. Wackermann, 1998: Validating a scatterometer wind algorithm for ERS-1 SAR. *IEEE Trans. Geosci. Remote Sens*., 36, 479–492.

Figa-Saldaña, J., J. J. W. Wilson, E. Attema, R. Gelsthorpe, M. R. Drinkwater, and A. Stoffelen, 2002: The advanced scatterometer (ASCAT) on the meteorological operational (MetOp) platform: a follow on for European wind scatterometers. *Can. J. Remote Sens*., 28, 404–412.

Fisher, C. M., G. S. Young, N. S. Winstead, and J. D. Haqq-Misra, 2008: Comparison of synthetic aperture radar-derived wind speeds with buoy wind speeds along the mountainous Alaskan coast. *J. Appl. Meteorol. Climatol.,* 47, 1365–1376.

Freilich, M. H., and R. S. Dunbar, 1999: The accuracy of the NSCAT-1 vector winds: comparisons with National Data Buoy Center buoys. *J. Geophys. Res*., 104, 11231–11246.

Gerling, T., 1986: Structure of the surface wind field from the SEASAT SAR. *J. Geophys. Res*., 91, 2308–2320.

Grubišić, V., R. B. Smith, and C. Schär, 1995: The effect of bottom friction on shallow-water flow past an isolated obstacle. *J. Atmos. Sci.*, 52, 1985–2005.

Grubišić, V., and B. J. Billings, 2008: Climatology of the Sierra Nevada mountain-wave events. *Mon. Wea. Rev.*, 136, 757–768.

Hersbach, H., A. Stoffelen, and S. de Haan, 2007: An improved C-band scatterometer ocean geophysical model function: CMOD5. *J. Geophs. Res.*, 112, doi:10.1029/2006JC003743.

Holt, B., 2004: SAR imaging of the ocean surface. *Synthetic aperture radar marine user's manual*, C. R. Jackson and J. R. Apel, Eds., NOAA/NESDIS Center for Satellite Applications and Research, 25–79.

Hong, S.-Y., and J.-O. J. Lim, 2006: The WRF single-moment 6-class microphysics scheme (WSM6). *J. Korean Meteorol.. Soc.*, 42, 129–151.

Hong, S.-Y., Y. Noh, and J. Dudhia, 2006: A new vertical diffusion package with an explicit treatment of entrainment processes. *Mon. Wea. Rev.*, 134, 2318–2341.

Horstmann, J., W. Koch, S. Lehner, and R. Tonboe, 2000: Wind retrieval over the ocean using synthetic aperture radar with C-band HH polarization. *IEEE Trans. Geosci. Remote Sens*., 38, 2122–2131.

Horstmann, J., J. Schiller, J. Schulz-Stellenfleth, and S. Lehner, 2003: Global wind speed retrieval from SAR. *IEEE Trans. Geosci. Remote Sens*., 41, 2277–2286.

Kain, J. S. 2004: The Kain-Fritsch convective parameterization: An update. *J. Appl. Meteorol.,* 43, 170–181.

Khurshid, S., D. Bradley, M. Manore, and C. Fogarty, 2012: National SAR winds project. Poster presentation, *33rd Canadian Symposium on Remote Sensing,* Ottawa, National SAR Winds Project ON, Canada*,* CRSS.

Koch, W., and F. Feser, 2006: Relationship between SAR-Derived Wind Vectors and Wind at 10-m Height Represented by a Mesoscale Model. *Mon. Wea. Rev.*, 134, 1505-1517.

Li, X., W. Zheng, X. Yang, Z. Li, and W. G. Pichel, 2011: Sea surface imprints of coastal mountain lee waves imaged by synthetic aperture radar. *J. Geophys. Res.*, 116 doi:10.1029/2010JC006643.

Mlawer, E. J., S. J. Taubman, P. D. Brown, M. J. Iacono, and S. A. Clough, 1997: Radiative transfer for inhomogeneous atmospheres: RRTM, a validated correlated-k model for the longwave. *J. Geophys. Re*s., 102, 16663–16682.

Monaldo, F. M., D. R. Thompson, R. C. Beal, W. G. Pichel, and P. Clemente-Colon, 2001: Comparison of SAR-derived wind speeds with model predictions and ocean buoy measurements. *IEEE Trans. Geosci. Remote Sens.*, 39, 2587–2600.

Monaldo, F. M., D. R. Thompson, W. G. Pichel, and P. Clemente-Colón, 2004: A systematic comparison of QuikSCAT and SAR ocean surface speeds. *IEEE Trans. Geosci. Remote Sens.*, 42, 283–291.

Pichel, W. G., F. Monaldo, C. Jackson, X. Li, J. Sapper, and X. Yang, 2011: NOAA operational SAR sea surface wind products. Proceedings, *Geoscience and Remote Sensing Symposium, 2011*, Vancouver, Canada, IEEE International, 1323–1326.

Schär, C., and R. B. Smith, 1993: Shallow-water flow past isolated topography. Part I: Vorticity production and wake formation. *J. Atmos. Sci*., 50, 1373–1400.

Schroeder, A. J., D. R. Stauffer, N. L. Seaman, A. Deng, A. M. Gibbs, G. K. Hunter, and G.S. Young, 2006: An automated high-resolution, rapidly relocatable meteorological nowcasting and prediction system. *Mon. Wea. Rev*., 134, 1237–1265.

Sikora, T. D., G. S. Young, M. D. Stepp, and C. M. Fisher, 2011: A synthetic aperture radar-based climatology of open cell convection over the Northeast Pacific Ocean. *J. Appl. Meteorol. Climatol.*, 50, 594–603.

Skamarock, W. C., J. B. Klemp, J. Dudhia, D. O. Gill, D. M. Barker, M. G. Duda, X.-Y. Huang, W. Wang, and J. Powers, 2008: A description of the advanced research WRF version 3. NCAR Technical Note NCAR/TN-475+STR, 125 pp.

Stoffelen, A., and D. L. T. Anderson, 1993: Wind retrieval and ERS-1 scatterometer radar backscatter measurements. *Adv. Space Res.*, 13, 53–60.

Stoffelen, A., and D. L. T. Anderson, 1997: Scatterometer data interpretation: estimation and validation of the transfer function CMOD4. *J. Geophys. Res.*, 102, 5767-5780.

Thompson, D. R. and R. C. Beal, 2000: Mapping high resolution wind fields using synthetic aperture radar. *Johns Hopkins APL Tech. Dig.*, 21, 58–67.

Thompson, D. R., F. M. Monaldo, W. G. Pichel, and P. Clemente-Colón, 2001: Combined estimates improve high-resolution coastal wind mapping. *EOS Trans., Am. Geophys. Union*, 82, 469.

Uhlhorn, E. W., P. G. Black, J. L. Franklin, M. Goodberlet, J. Carswell, and A. S. Goldstein, 2007: Hurricane surface wind measurements from an operational stepped frequency microwave radiometer. *Mon. Wea. Rev.*, 135, 3070–3085.

Wackermann, C. C., C. L. Rufenach, R. A. Schuchman, J. A. Johannesen, and K. L. Davidson, 1996: Wind vector retrieval using ERS-1 synthetic aperture radar imagery. *J. Geophys. Res*., 34, 1343–1352.

Wedam, G. B., L. A. McMurdie, and C. F. Mass, 2009: Comparison of model forecast skill of sea level pressure along the east and west coasts of the United States. *Wea. Forecasting*, 24, 843–854.

Wetzel, M. A., S. K. Chai, M. J. Szumowski, W. T. Thompson, T. Haack, G. Vali, and R. Kelly, 2001: Evaluation of COAMPS forecasts of coastal stratus using satellite microphysical retrievals and aircraft measurements. *Wea. Forecasting*, 16, 588–599.

Wilks, D. S., 2011: *Statistical Methods in the Atmospheric Sciences.* 3rd ed. Academic Press, 676 pp.

Young, G. S., T. D. Sikora, and C. M. Fisher, 2007: Use of MODIS and synthetic aperture radar wind speed imagery to describe the morphology of open cell convection. *Can. J. Remote Sens*., 33, 357–367.